

Cite this: *RSC Adv.*, 2019, 9, 38280

# Preparation and evaluation of a hierarchical Bi<sub>2</sub>MoO<sub>6</sub>/MSB composite for visible-light-driven photocatalytic performance

Lu Cai,<sup>a</sup> Yarui Zhou,<sup>b</sup> Zhen Wang,<sup>c</sup> Jinlong Chen,<sup>d</sup> Lili Ji,<sup>e</sup> Jian Guo,<sup>f</sup> Yaning Wang,<sup>e</sup> Wendong Song<sup>d</sup> and Jianshe Liu<sup>g,\*a</sup>

In this study, waste mussel shells were used to remove dyes in aqueous solution. Mussel shell was prepared into mussel shell biochar (MSB), which was used as a carrier to support Bi<sub>2</sub>MoO<sub>6</sub>. A novel Bi<sub>2</sub>MoO<sub>6</sub>/MSB composite photocatalyst was developed by the hydrothermal synthesis method. The as-synthesized sample was characterized by X-ray diffraction (XRD), scanning electron microscopy (SEM), N<sub>2</sub> adsorption–desorption method, Fourier transform infrared spectroscopy (FTIR) and UV-vis diffuse reflectance spectra (DRS). Then, the photocatalytic activity of the prepared samples was determined by testing the photodegradation of Rhodamine B (RhB) under visible-light ( $\lambda > 420$  nm) irradiation. The pre exfoliated layered MSB was an excellent supporting matrix for the growth of Bi<sub>2</sub>MoO<sub>6</sub> nanoflakes. The obtained hierarchical Bi<sub>2</sub>MoO<sub>6</sub>/MSB composites exhibited significantly enhanced performance for photocatalytic degradation of RhB compared with pure Bi<sub>2</sub>MoO<sub>6</sub> under visible light irradiation because of the improved electron–hole pair separation, which boosted the number of exposed catalytic active sites. Moreover, the Bi<sub>2</sub>MoO<sub>6</sub>/MSB composite photocatalyst is of good stability and reusability.

Received 22nd August 2019  
Accepted 4th November 2019

DOI: 10.1039/c9ra06559h

rsc.li/rsc-advances

## 1. Introduction

With the high speed of industrialization, dyes have become a major source of water pollution as they are widely used in such fields as the textile, tannery, printing, paper, plastic and cosmetic industries.<sup>1,2</sup> Due to the improvement of people's requirements on color, various dyes with the abilities of oxidation resistance, photolysis resistance or biodegradation resistance have sprung up, which are difficult to be treated with traditional water treatment systems. Some dyes are carcinogenic, mutagenic, and teratogenic, and even their products may be carcinogenic or otherwise toxic after being transformed or degraded, such as aromatic amines.<sup>3–5</sup> Moreover, dye effluents discharged into water even at low concentrations could threaten the aquatic animals and plants, and destroy the ecological environment. Thus, the efficient treatment of dyestuff wastewater has always been a hot topic. Various methods had been

applied to degrade dyes including chemical oxidation, micro-biological degradation, electrochemical treatment, adsorption, photocatalytic degradation, *etc.*<sup>6–9</sup> In recent years, there has been considerable interest in the utilization of photocatalysis systems for the destruction of dyes, so more and more efficient photocatalysts have been developed. Remarkably, visible-light-driven photocatalysis has received much attention as an economical and practical method. Bismuth-based photocatalysts such as Bi<sub>2</sub>MoO<sub>6</sub>, BiVO<sub>4</sub>, BiOX (X = Br, Cl), Bi<sub>2</sub>WO<sub>6</sub>, Bi<sub>2</sub>Fe<sub>4</sub>O<sub>9</sub> and Bi<sub>2</sub>O<sub>2</sub>CO<sub>3</sub>,<sup>10–14</sup> possessing excellent photocatalytic activity under visible-light irradiation, have become representative photocatalytic materials.<sup>15–18</sup> Besides, Bi<sub>2</sub>MoO<sub>6</sub> is considered as an ideal photocatalyst from the viewpoint of using visible light.<sup>19–21</sup> However, the practical application of individual phase Bi<sub>2</sub>MoO<sub>6</sub> is still limited by its dissatisfactory quantum yield.<sup>22</sup> In order to further improve the photocatalytic performance of Bi<sub>2</sub>MoO<sub>6</sub>, previous studies have attempted to immobilize the photocatalyst onto various supports such as activated carbon, graphene, carbon nanotubes, zeolite, glass, and silica; however, they exhibited high cost and lack of treatability.<sup>23–29</sup>

Mussel shell, as a by-product of the aquaculture industry, is an abundant residual source of carbonate. As we all know, shell is a kind of well-arranged organic–inorganic composite material formed under the control of organic macromolecules. Shell has a unique multi-scale and multi-level “brick-mud” assembly structure and is a kind of cheap biological material. After modification by simple heat treatment, the organic matter in the mussel shell can be decomposed and released, resulting in

<sup>a</sup>College of Environmental and Science Technology, Donghua University, Shanghai 201620, China. E-mail: liujianshe@dhu.edu.cn<sup>b</sup>College of Naval Architecture and Mechanical-Electrical Engineering, Zhejiang Ocean University, Zhoushan 316022, China<sup>c</sup>College of Marine Science and Technology, Zhejiang Ocean University, Zhoushan 316022, China<sup>d</sup>College of Petrochemical and Energy Engineering, Zhejiang Ocean University, Zhoushan 316022, China<sup>e</sup>Institute of Innovation & Application, Zhejiang Ocean University, Zhoushan 316022, China<sup>f</sup>College of Food and Medical, Zhejiang Ocean University, Zhoushan 316022, China

the formation of porous biochar skeleton, which is expected to be a low cost and effective carrier material. The biochar had excellent conductivity, which would lower quick recombination of electrons and electron holes during the photocatalysis for enhancing photocatalytic degradation. Efficient attachment of photocatalyst onto the biochar is allowed due to the large specific surface area, rich functional groups and easy surface modification of the biochar.<sup>30</sup>

Therefore, the present study suggested a biochar-support  $\text{Bi}_2\text{MoO}_6$  as an effective photocatalyst to eliminate dyes in water. The effect of biochar-support  $\text{Bi}_2\text{MoO}_6$  on photocatalytic activity was investigated by decomposing Rhodamine B (RhB) under visible-light irradiation. The possible photocatalytic mechanism of this composite was also discussed. The as-prepared sample may be expected to be a cheap and efficient photocatalyst, which could realize the value-added use of waste mussel shells.

## 2. Materials and methods

### 2.1 Materials

The mussel shells were collected at Shengsi, Zhejiang province, China.  $\text{Bi}(\text{NO}_3)_3 \cdot 5\text{H}_2\text{O}$ ,  $\text{Na}_2\text{MoO}_4 \cdot 2\text{H}_2\text{O}$ ,  $\text{C}_2\text{H}_5\text{OH}$  and  $\text{C}_2\text{H}_6\text{O}_2$  were purchased from Sinopharm Chemical Reagent Co., Ltd., in Shanghai, China.  $\text{RhB}(\text{C}_{28}\text{H}_{31}\text{ClN}_2\text{O}_3)$  was purchased at Beijing Chemical Reagent Co. Ltd., in Beijing, China. All chemicals were analytical grade and used as received without further purification.

### 2.2 Preparation of composite photocatalyst

The mussel shells were washed to remove dirt from its surface, treated with 0.1% HCl for 24 h, then washed with distilled water until neutral and dried at 80 °C. The dried mussel shells loaded in corundum crucible were placed in a tube furnace (Shanghai Jyjing Precision Instrument Manufacturing Co., Ltd., Shanghai, China). It was heated at a rate of 10 °C  $\text{min}^{-1}$  from room temperature to 900 °C under purified nitrogen (99.99%) flow of 100 mL  $\text{min}^{-1}$ . Next, the calcination step was held for 3 h at 900 °C. The calcined sample was then cooled to room temperature under nitrogen flow and grounded into powder, which was labelled as MSB.

The  $\text{Bi}_2\text{MoO}_6$ /MSB composite photocatalyst were synthesized through the hydrothermal method. Briefly,  $\text{Bi}(\text{NO}_3)_3 \cdot 5\text{H}_2\text{O}$  (0.3630 g) and  $\text{Na}_2\text{MoO}_4 \cdot 2\text{H}_2\text{O}$  (0.0907 g) were completely dissolved in two different 7 mL glycol, respectively. 0.1306 g MSB (the mass ratio of  $\text{Bi}_2\text{MoO}_6$  to MSB was 1.75) were dissolved in 20 mL ethyl alcohol. After stirring for 30 min, the three solutions were transferred into a 50 mL Teflon-lined stainless autoclave, heated at 160 °C for 12 h in an oven, and then cooled down to room temperature. The resulting mixture was washed with deionized water and ethyl ethanol to remove any ionic residual, and dried in an oven at 60 °C for 6 h in an oven, named as  $\text{Bi}_2\text{MoO}_6$ /MSB. By adjusting the mass ratio of  $\text{Bi}_2\text{MoO}_6$  to BMS, a series of  $\text{Bi}_2\text{MoO}_6$ /MSB with different mass ratio (0.25, 0.75, 1.25, 1.75 and 2.25) were obtained and named as B/M-0.25, B/M-0.75, B/M-1.25, B/M-1.75, and B/M-2.25, respectively.

### 2.3 Characterization

FTIR spectra were obtained using a PerkinElmer Fourier transform infrared (Nicoletteis 50, Thermo Fourier, Waltham, MA, USA) spectrometer with KBr as a diluting agent and operated in the frequency range of 4000–500  $\text{cm}^{-1}$ . The crystal structures of the as-prepared sample were investigated by XRD analysis at room temperature on an XRD powder diffraction instrument (D/max2500, Shimadzu Co., Ltd., Kyoto, Japan) in the range of  $2\theta$  from 20° to 80°. Specific surface area measurements were performed on a micromeritics ASAP 2010 instrument (Micromeritics Instrument Ltd., Atlanta, GA, USA) and analysed by the BET method. The morphology change of the sample was studied by a scanning electron microscopy (SEM, Hitachi-4800, Hitachi Co., Ltd., Tokyo, Japan). The optical properties of the samples were determined by the Shimadzu UV 2600 spectrophotometer (Shimadzu Co., Ltd., Kyoto, Japan) in the wavelength range of 200–800 nm.

### 2.4 Photocatalytic activity

The photocatalytic performance of the sample was evaluated for the degradation of RhB under visible-light irradiation. A 300 W Xe lamp combined with a 400 nm cutoff filter was used as a light source and its distance to the liquid surface of the suspension was about 10 cm. The temperature of the reaction system was kept at 25 °C by cycling water. In the experiment, 0.02 g photocatalyst was added to 50 mL of 6  $\text{mg L}^{-1}$  RhB solution. Prior to irradiation, the suspensions were stirred in the dark for 3 h to establish an adsorption-desorption equilibrium. During irradiation, 2 mL liquid was taken from the suspension at 10, 20, 30, 60, 90 and 120 min followed by the separation of photocatalyst through centrifugation. The absorbance of RhB solution without catalyst was determined at 554 nm using a spectrophotometer (UV 2600, Shimadzu Co., Ltd., Kyoto, Japan). The degradation rate ( $D\%$ ) was calculated by the eqn (1):

$$D\% = \frac{A_0 - A_t}{A_0} \times 100\% \quad (1)$$

where  $A_0$  was the initial absorbance value of RhB solution and  $A_t$  was the absorbance value of RhB the solution after light irradiation.

The stability experiment was carried out by the degradation of RhB solution (50 mL, 6  $\text{mg L}^{-1}$ ) over  $\text{Bi}_2\text{MoO}_6$ /MSB for four successive cycles. After each cycle, the catalyst was separated and collected by centrifugation, then was washed with deionized water and dried. After that, it was added into the fresh RhB solution (50 mL, 6  $\text{mg L}^{-1}$ ) to initiate the reaction.

## 3. Results and discussion

### 3.1 Materials characterization

Fig. 1 illustrates the FTIR spectra of MSB,  $\text{Bi}_2\text{MoO}_6$ , and  $\text{Bi}_2\text{MoO}_6$ /MSB. As can be seen from Fig. 1(a), the MSB spectra has a strong and wide peak at 1425  $\text{cm}^{-1}$ , a narrow peak at 874  $\text{cm}^{-1}$  and a weak and narrow peak at 711  $\text{cm}^{-1}$ , corresponding to the asymmetric stretching vibration peak, in-plane bending vibration peak and out-of-plane bending vibration



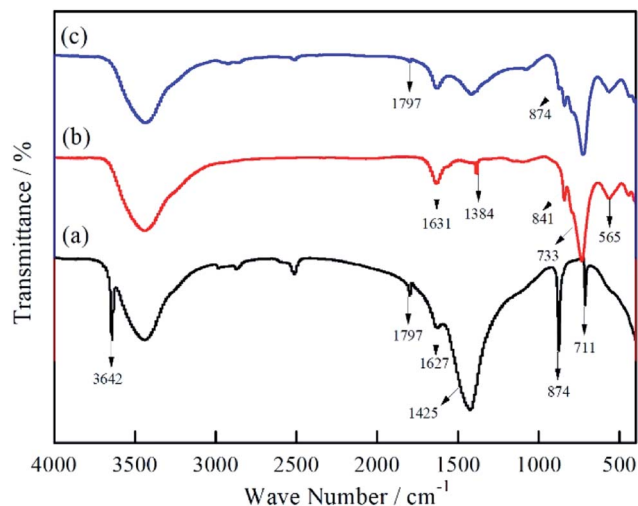


Fig. 1 FTIR spectra of MSB, pure  $\text{Bi}_2\text{MoO}_6$  and  $\text{Bi}_2\text{MoO}_6/\text{MSB}$  composite catalyst ((a) MSB; (b)  $\text{Bi}_2\text{MoO}_6$ ; (c)  $\text{Bi}_2\text{MoO}_6/\text{MSB}$ ).

peak of  $\text{CO}_3^{2-}$  group, respectively.<sup>31</sup> The absorption peak at  $1797\text{ cm}^{-1}$  is the vibration peak of  $\text{C}=\text{O}$  in the  $\text{CO}_3^{2-}$  group.<sup>32</sup> The above peaks are characteristic peaks of carbonate minerals, which coincide with the characteristic peaks of  $\text{CaCO}_3$ . In addition, the absorption peak at  $3642\text{ cm}^{-1}$  is the stretching vibration peak of  $-\text{OH}$ , which indicates the existence of  $\text{Ca}(\text{OH})_2$  in MSB.<sup>33</sup>

Fig. 1(b) shows the infrared spectrum of pure  $\text{Bi}_2\text{MoO}_6$ , the band at  $1384\text{ cm}^{-1}$  is the vibration of the  $\text{Bi}-\text{O}$  bond, and the absorption bands at  $841\text{ cm}^{-1}$ ,  $733\text{ cm}^{-1}$  and  $565\text{ cm}^{-1}$  correspond to the  $\text{Mo}=\text{O}$  stretching vibration,  $\text{MoO}_6$  asymmetric stretching and  $\text{MoO}_6$  flexural vibration.<sup>34,35</sup> As shown in Fig. 1(c), all characteristic absorption peaks of  $\text{Bi}_2\text{MoO}_6$  can be observed in the  $\text{Bi}_2\text{MoO}_6/\text{MSB}$  curve, and  $\text{CaCO}_3$  characteristic absorption peaks are found at  $1797$  and  $874\text{ cm}^{-1}$ , indicating the existence of  $\text{Bi}_2\text{MoO}_6$  and MSB.

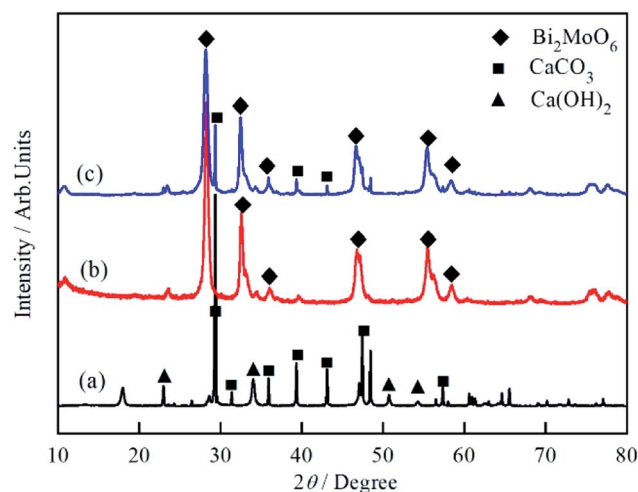


Fig. 2 XRD patterns of MSB, pure  $\text{Bi}_2\text{MoO}_6$  and  $\text{Bi}_2\text{MoO}_6/\text{MSB}$  composite catalyst ((a) MSB; (b)  $\text{Bi}_2\text{MoO}_6$ ; (c)  $\text{Bi}_2\text{MoO}_6/\text{MSB}$ ).

The XRD patterns of MSB,  $\text{Bi}_2\text{MoO}_6$  and  $\text{Bi}_2\text{MoO}_6/\text{MSB}$  composites are shown in Fig. 2. The profile in Fig. 2(a) confirms that pure MSB consists of the calcite type of  $\text{CaCO}_3$  (JCPDS 83-1762) and hexagonal phase of  $\text{Ca}(\text{OH})_2$  (JCPDS 04-0733). The existence of  $\text{Ca}(\text{OH})_2$  is mainly because high temperature decomposes  $\text{CaCO}_3$  into  $\text{CaO}$ , which reacts with  $\text{H}_2\text{O}$  in the air to form  $\text{Ca}(\text{OH})_2$ . Fig. 2(b) confirms that the as-prepared sample is phase-pure orthorhombic  $\text{Bi}_2\text{MoO}_6$ , which is consistent with the reported result (JCPDS 76-2388). As shown in Fig. 2(c), the main diffraction peaks of  $\text{Bi}_2\text{MoO}_6/\text{MSB}$  at about  $23.3^\circ$ ,  $28.1^\circ$ ,  $32.3^\circ$ ,  $35.8^\circ$ ,  $46.7^\circ$ ,  $55.3^\circ$  and  $58.2^\circ$  could be perfectly indexed to the (111), (131), (200), (151), (062), (331) and (191) crystal planes of  $\text{Bi}_2\text{MoO}_6$ , which consistent with pure  $\text{Bi}_2\text{MoO}_6$ . At the same time, the diffraction peaks of MSB located at  $2\theta = 29.4^\circ$ ,  $39.5^\circ$ , and  $43.1^\circ$  could be obviously observed, corresponding to the (104), (202) and (024) crystal planes of calcite type  $\text{CaCO}_3$  (JCPDS 83-1762). The results showed that the characteristic peaks of MSB and  $\text{Bi}_2\text{MoO}_6$  were observed, which indicates that  $\text{Bi}_2\text{MoO}_6$  was successfully combined with MSB.

The morphology of the sample was characterized by SEM. As shown in Fig. 3, MSB is a nano-flake structure with different size holes, which is a porous calcium compound skeleton formed by organic matter escaping from shells after high-temperature treatment. Pure  $\text{Bi}_2\text{MoO}_6$  is a hollow spherical structure composing of nanosheets, with a diameter of about  $1.5\text{--}2\text{ }\mu\text{m}$ . Compared with pure  $\text{Bi}_2\text{MoO}_6$ , the nanomorphology of  $\text{Bi}_2\text{MoO}_6$  in the composite catalyst is changed. In the composite photocatalyst, the hollow spherical structure of  $\text{Bi}_2\text{MoO}_6$  is missing, and the  $\text{Bi}_2\text{MoO}_6$  nanosheets attached to MSB surface form an obvious hierarchical structure. Moreover, after hydrothermal treatment, the particles of the MSB in the composite photocatalyst become smaller and the hierarchical structure becomes more obvious.

The specific surface areas, pore volumes and average pore diameters of MSB,  $\text{Bi}_2\text{MoO}_6$ , and  $\text{Bi}_2\text{MoO}_6\text{--MSB}$  are shown in Table 1. Compared with pure  $\text{Bi}_2\text{MoO}_6$ , the surface area, pore volume and average pore diameter of  $\text{Bi}_2\text{MoO}_6/\text{MSB}$  composite decrease, because the addition of MSB changes the self-assembly structure of  $\text{Bi}_2\text{MoO}_6$  nanosheets, which is deposited on the surface and pores of MSB. Moreover, the specific surface area of the  $\text{Bi}_2\text{MoO}_6/\text{MSB}$  composite gradually decreased with the increase of MSB addition. According to Fig. 4, the nitrogen adsorption isotherm of  $\text{Bi}_2\text{MoO}_6/\text{MSB}$  (B/M-1.75) accords with type IV adsorption isotherm with a hysteresis loop at pressure ( $P/P_0 > 0.8$ ), indicating that there may be a certain number of mesoporous in composite photocatalyst.<sup>36</sup> The pore size distribution of  $\text{Bi}_2\text{MoO}_6/\text{MSB}$  also reflects the above results, mainly in the range of  $2\text{--}20\text{ nm}$ .

The difference in optical absorption could highly affect the photocatalytic performance of the sample. Fig. 5 exhibits the UV-vis diffuse reflectance spectra of MSB,  $\text{Bi}_2\text{MoO}_6$  and  $\text{Bi}_2\text{MoO}_6/\text{MSB}$  are various due to their different photo-absorption properties from UV light region to visible light region. Pure  $\text{Bi}_2\text{MoO}_6$  and  $\text{Bi}_2\text{MoO}_6/\text{MSB}$  all show significantly absorbance in the visible-light region ( $\lambda > 400\text{ nm}$ ). The obtained diffuse reflectance spectra are further used to determine their optical band gap energies with the formula  $(\alpha h\nu)^2 = A(h\nu -$





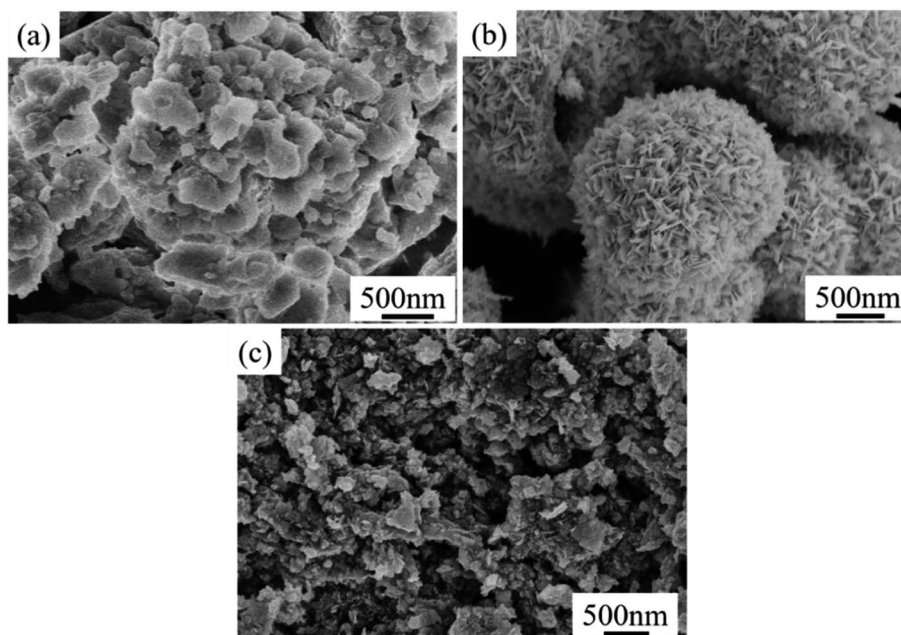


Fig. 3 SEM of  $\text{Bi}_2\text{MoO}_6/\text{MSB}$  composite catalyst, pure  $\text{Bi}_2\text{MoO}_6$  and MSB ((a) MSB; (b)  $\text{Bi}_2\text{MoO}_6$ ; (c)  $\text{Bi}_2\text{MoO}_6/\text{MSB}$ ).

$E_g$ ), where  $\alpha$ ,  $\nu$ ,  $A$  and  $E_g$  are the absorption coefficient, the incident light frequency, a constant and the band gap energy. The band gap energies of  $\text{Bi}_2\text{MoO}_6$  and  $\text{Bi}_2\text{MoO}_6/\text{MSB}$  could be evaluated from a plot of  $(\alpha h\nu)^2$  vs.  $h\nu$  as presented in Fig. 5 (inset). The estimated band gap energies for the  $\text{Bi}_2\text{MoO}_6$  and  $\text{Bi}_2\text{MoO}_6/\text{MSB}$  were about 2.65 and 3.00 eV, respectively.

### 3.2 Photocatalytic activity

The photocatalytic activity of the as-prepared catalysts was evaluated for the photocatalytic degradation of RhB under visible light irradiation. The dark adsorption data was shown in Fig. 6(a), the adsorption equilibrium between the photocatalyst and the dye solution has established. As is illustrated in Fig. 6(b), when the RhB suspension was irradiated with visible light for 120 min in the absence of any photocatalyst, no obvious change can be observed in the RhB solution; therefore, the photodegradation of RhB can be neglected in this study. Under the same conditions, 11.0% RhB is degraded by MSB

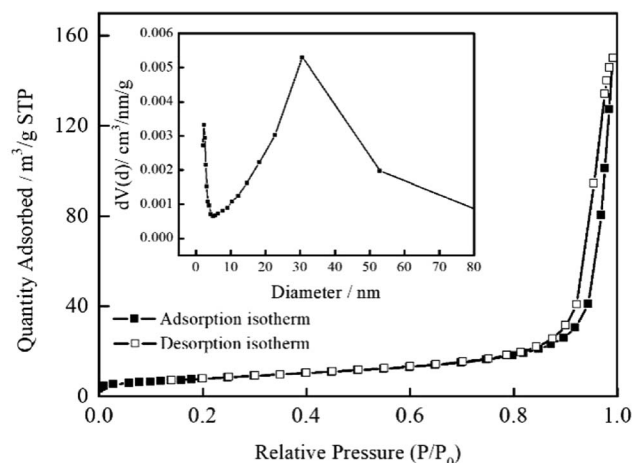


Fig. 4  $\text{N}_2$  sorption isotherms of  $\text{Bi}_2\text{MoO}_6/\text{MSB}$  (B/M-1.75) and corresponding pore size distribution (inset). (According to the following performance tests  $\text{Bi}_2\text{MoO}_6/\text{MSB}$  (B/M-1.75) showed the best photocatalytic performance.).

Table 1 Specific surface areas, total pore volumes and average pore diameters of MSB, pure  $\text{Bi}_2\text{MoO}_6$  and  $\text{Bi}_2\text{MoO}_6/\text{MSB}$  composite catalyst

Samples	BET ( $\text{m}^2 \text{g}^{-1}$ )	Total pore volume ( $\text{cm}^3 \text{g}^{-1}$ )	Average pore diameter (nm)
MSB	2.47	0.004	6.53
$\text{Bi}_2\text{MoO}_6$	43.15	0.183	16.98
$\text{Bi}_2\text{MoO}_6/\text{MSB}$ (B/M-2.25)	32.36	0.110	8.18
$\text{Bi}_2\text{MoO}_6/\text{MSB}$ (B/M-1.75)	28.64	0.069	9.63
$\text{Bi}_2\text{MoO}_6/\text{MSB}$ (B/M-1.25)	27.63	0.076	8.79
$\text{Bi}_2\text{MoO}_6/\text{MSB}$ (B/M-0.75)	20.59	0.042	8.15
$\text{Bi}_2\text{MoO}_6/\text{MSB}$ (B/M-0.25)	18.48	0.036	8.97



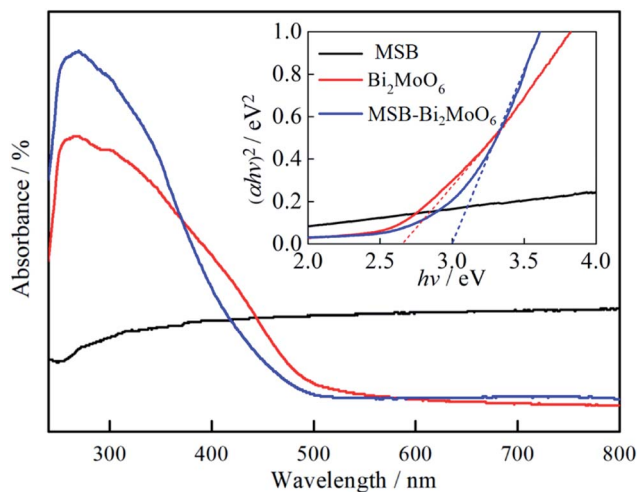


Fig. 5 UV-vis spectra of MSB, pure  $\text{Bi}_2\text{MoO}_6$  and  $\text{Bi}_2\text{MoO}_6/\text{MSB}$  composite catalyst.

after 120 min visible light illumination, which indicates that MSB has the photocatalytic activity against RhB.

The degradation efficiency of pure  $\text{Bi}_2\text{MoO}_6$  was 69.2%. Furthermore, it is worth noting that the combination of a certain amount of MSB with  $\text{Bi}_2\text{MoO}_6$  (mass ratio = 1.75) result in a sharp increase of RhB degradation from 69.2% to

94.4%. The improvement of photocatalytic activity of  $\text{Bi}_2\text{MoO}_6/\text{MSB}$  can be attributed to the following reasons.  $\text{Bi}_2\text{MoO}_6$  was deposited on the surface or in the pore of MSB, which could cover or block the pores of MSB, leading to a decrease in the specific surface area of composite materials. However,  $\text{Bi}_2\text{MoO}_6$  is dispersed on MSB carrier, so as to expose more photocatalytic activity sites, which leads to the improvement of photocatalytic activity of composite materials. Besides, as is known, mussel shell has abundant transition metal elements, so MSB internally contains transition metal oxides,<sup>37</sup> acting as photo-generated holes and electrons traps, which hinder the recombination of hole–electron pairs, and significantly improve the photocatalytic activity of  $\text{Bi}_2\text{MoO}_6/\text{MSB}$ . The forbidden bandwidth of  $\text{Bi}_2\text{MoO}_6/\text{MSB}$  is larger than that of the pure  $\text{Bi}_2\text{MoO}_6$ , indicating it needs more energy to activate, however, it has higher efficiency of light utilization, shows significantly absorbance in the visible-light region, and exhibits an enhanced photocatalytic activity.

The degradation process follows pseudo-first-order kinetics, as clearly shown in Fig. 6(c). The degradation rate of RhB over  $\text{Bi}_2\text{MoO}_6/\text{MSB}$  is much faster than other samples, and the apparent rate constant  $k$  of the composite is  $0.02568 \text{ min}^{-1}$ , which is 2.44 times of that over pure  $\text{Bi}_2\text{MoO}_6$ . Moreover, compared with some previous reports (Table 2), the  $K$  value of present  $\text{Bi}_2\text{MoO}_6/\text{MSB}$  is somehow higher than other semiconductor composites in previous reports, such as  $\text{Bi}_2\text{MoO}_6$  with

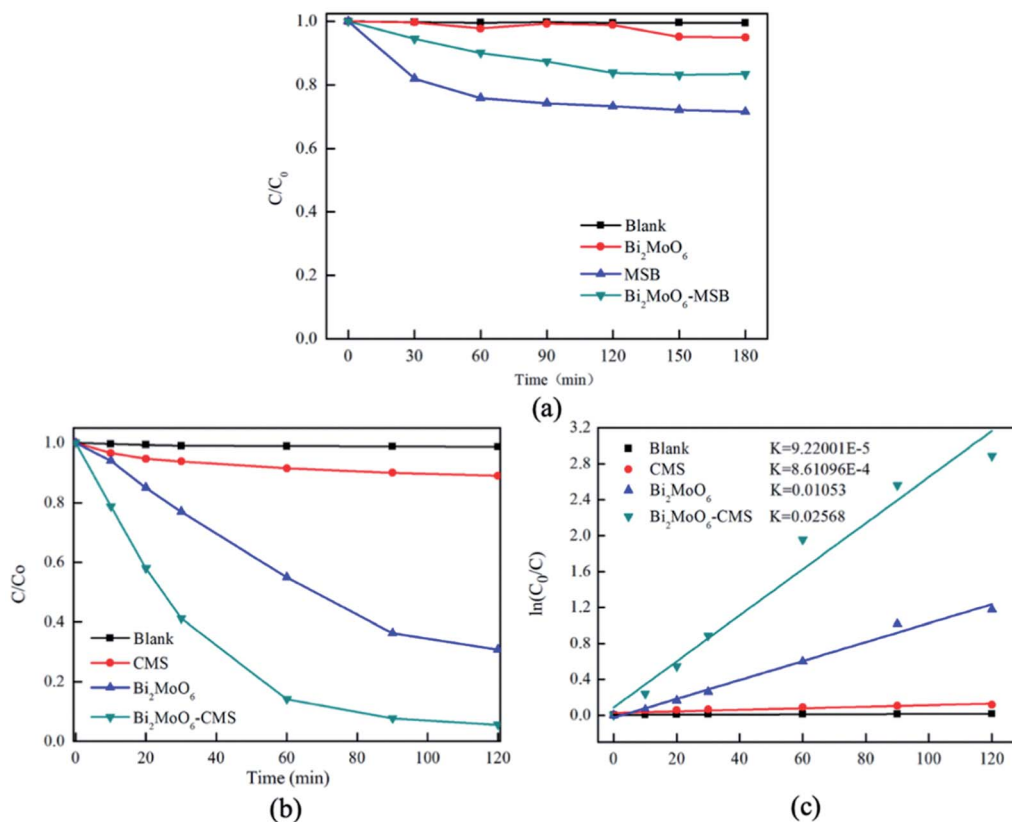


Fig. 6 (a) Dark adsorption equilibrium curve of MSB, pure  $\text{Bi}_2\text{MoO}_6$  and  $\text{Bi}_2\text{MoO}_6/\text{MSB}$  composite catalyst respectively; (b) degradation rate of RhB by MSB, pure  $\text{Bi}_2\text{MoO}_6$  and  $\text{Bi}_2\text{MoO}_6/\text{MSB}$  composite catalyst respectively; (c) kinetic analysis for the degradation of the RhB.



Table 2 *K* value of different photocatalyst composites in literatures and this work

Photocatalyst	Light source	Catalyst conc. (mg mL <sup>-1</sup> )	Dye	Dye conc.	Irradiation time (min)	<i>K</i> (min <sup>-1</sup> )	Reference
Bi <sub>2</sub> MoO <sub>6</sub> /MSB	300 W Xe lamp	0.4	RhB	6 mg L <sup>-1</sup>	120	0.02568	This work
Bi <sub>2</sub> MoO <sub>6</sub>	10 000 K Xe lamp	1	RhB	5 mg L <sup>-1</sup>	300	0.022	37
Bi <sub>2</sub> MoO <sub>6</sub> /graphene	500 W Xe lamp	0.5	MB	1 × 10 <sup>-5</sup> M	120	0.0136	38
Bi <sub>2</sub> MoO <sub>6</sub> /CNTs/g-C <sub>3</sub> N <sub>4</sub>	500 W Xe lamp	1	2,4-DBP	20 mg L <sup>-1</sup>	120	0.0078	39
SnO <sub>2</sub> /Bi <sub>2</sub> MoO <sub>6</sub>	400 W halogen lamp	1	RhB	10 mg L <sup>-1</sup>	150	0.02831	40

$K = 0.022 \text{ min}^{-1}$ , Bi<sub>2</sub>MoO<sub>6</sub>/graphene with  $K = 0.0136 \text{ min}^{-1}$ , Bi<sub>2</sub>MoO<sub>6</sub>/CNTs/g-C<sub>3</sub>N<sub>4</sub> with  $K = 0.0078 \text{ min}^{-1}$ .<sup>38–40</sup> Although the *K* value of SnO<sub>2</sub>/Bi<sub>2</sub>MoO<sub>6</sub> is slightly higher than Bi<sub>2</sub>MoO<sub>6</sub>/MSB, the catalyst cost in this study is lower.<sup>41</sup> All the results showed that Bi<sub>2</sub>MoO<sub>6</sub>/MSB composite photocatalyst was a kind of high efficient photocatalyst with high degradation activity against RhB.

To further study the photocatalytic process of RhB, the UV-vis spectra of the RhB solution as a function of visible light irradiation time in the presence of Bi<sub>2</sub>MoO<sub>6</sub>/MSB is shown in Fig. 7. The main peak wavelength of the degrade solution gradually shifts from 554 nm to 497 nm as the irradiation time increases. Studies has shown that the blue-shift of the absorption band is caused by de-ethylation of RhB because of the attack by one of the active oxygen species on the *N*-ethyl group. When the de-ethylated process is fully completed, the absorption band shifts to 497 nm and RhB is turned to rhodamine. Rhodamine is then gradually decomposed due to the further destruction of the conjugated structure.<sup>42–45</sup>

Fig. 8 shows the results of photocatalytic efficiency of degradation of RhB solution by Bi<sub>2</sub>MoO<sub>6</sub>/MSB with different mass ratio. Fig. 8(a) exhibit the dark adsorption data of different photocatalyst, the adsorption equilibrium between the photocatalyst and the dye solution was reached. As shown in Fig. 8(b), it is obvious that the degradation efficiency increases gradually as the content of Bi<sub>2</sub>MoO<sub>6</sub> increase in the composite photocatalysts from B/M-0.25 to B/M-1.75 and the degradation

efficiency of B/M-1.75 reaches the highest (94.4%). However, the degradation efficiency of B/M-2.25 decreases to 48.5% in comparison with the B/M-1.75. This is because too much Bi<sub>2</sub>MoO<sub>6</sub> is prone to agglomerate, resulting in the effective adsorption sites and photolytic active sites of photocatalysts are reduced.<sup>46</sup> Fig. 8(c) is the degradation kinetics of RhB degradation by Bi<sub>2</sub>MoO<sub>6</sub>/MSB in different mass ratios. As can be seen from Fig. 8(c),  $\ln(C_0/C)$  and *t* showed a good linearity relationship. Compared with other samples, B/M-1.75 exhibits the excellent visible light catalytic activity with the *k* value of  $0.02568 \text{ min}^{-1}$ .

As is well known, the solution pH value plays an important role in the photocatalytic degradation of organic pollutants. The effect of pH on the photodegradation of RhB was studied in the pH range of 3–12. As shown in Fig. 9, with the increase of pH, the degradation rate of RhB increase firstly and then decrease. It can be observed that the optimum pH is 7 in the highest degradation rate (96%). Under the acidic conditions, the H<sup>+</sup> in solution will react with carbonyl, hydroxyl and other oxygen-containing functional groups on MSB surface, resulting in reducing the number of active contact sites and weakening adsorption and catalytic capacity. When the pH value is more than 7, the OH<sup>-</sup> in solution will compete with MSB surfactant functional group for adsorption, causing increasing repulsive force between the composite catalyst and organic dye molecules; therefore, it is not conducive to the adsorption of the catalyst on RhB, leading to a decrease of degradation ability.

Furthermore, the stability and reusability of the composite photocatalyst were also tested. As shown in Fig. 10, after four successive cycles of RhB degradation experiments, the photocatalytic degradation efficiency exhibits only a slight decrease from initial 94.4% for the first run to 82.7% for the fourth run. The XRD pattern of the used Bi<sub>2</sub>MoO<sub>6</sub>/MSB composite further confirm that there no obvious changes in the crystalline phase after recycling reactions, implying Bi<sub>2</sub>MoO<sub>6</sub>/MSB composite has better stability and reusability. Thus, Bi<sub>2</sub>MoO<sub>6</sub>/MSB composite is a good candidate for photocatalytic degradation of persistent organic pollutants in solution under visible light irradiation.

### 3.3 Photocatalytic mechanism

As is well known, photoinduced holes (h<sup>+</sup>), superoxide radicals (·O<sub>2</sub><sup>-</sup>) and hydroxyl radicals (·OH) are extremely active in photocatalytic reaction, which results in the degradation of organic pollutants.<sup>47–50</sup> In order to clarify the photocatalytic mechanism, it is vital to identify the main oxidants in the

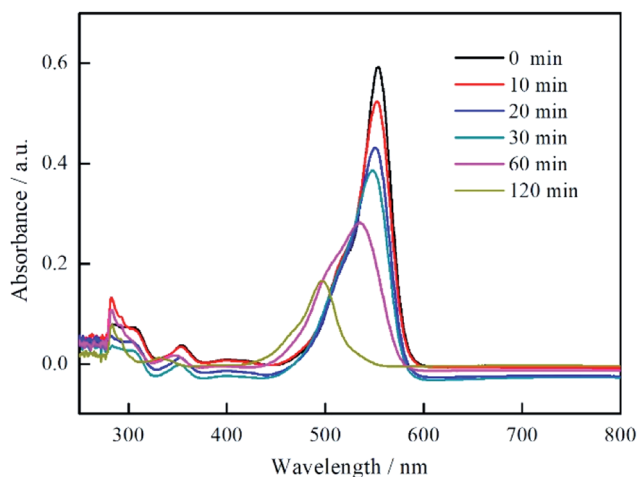


Fig. 7 UV absorption spectrum curves of RhB solution with Bi<sub>2</sub>MoO<sub>6</sub>/MSB as photocatalyst under visible light irradiation at different time.



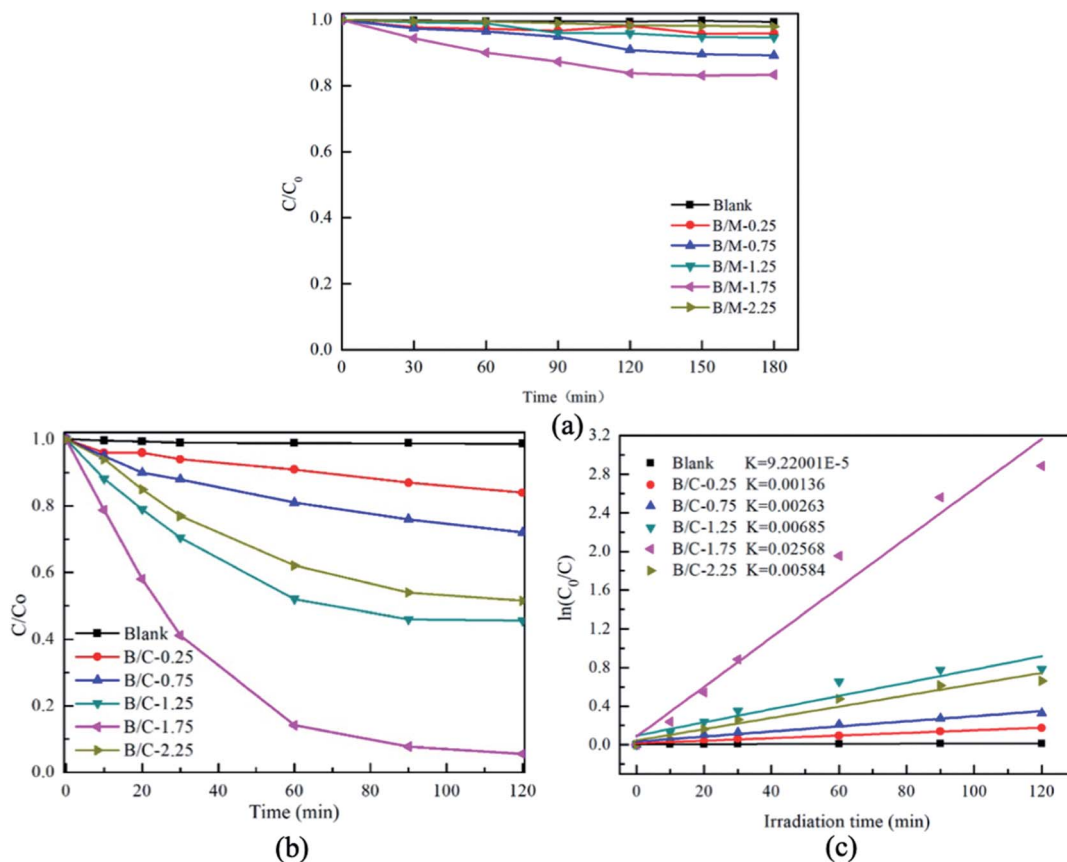


Fig. 8 (a) Dark adsorption equilibrium curve of MSB, pure  $\text{Bi}_2\text{MoO}_6$  and  $\text{Bi}_2\text{MoO}_6/\text{MSB}$  composite catalyst respectively; (b) comparison of the activity of  $\text{Bi}_2\text{MoO}_6/\text{MSB}$  composite photocatalyst with different loadings for the degradation of RhB; (c) kinetic analysis for the degradation of the RhB.

photodegradation process. In this study, sodium oxalate, *p*-benzoquinone, and isopropyl alcohol are used as  $\text{h}^+$ ,  $\cdot\text{O}_2^-$  and  $\cdot\text{OH}$  scavenger, respectively and their effects on the photocatalytic degradation of RhB are shown in Fig. 11. As is illustrated in Fig. 11, the degradation efficiency of RhB decreases from 94.4% to 31.2%, 22.6% and 55.7% by adding

photoinduced holes, superoxide radicals, and hydroxyl radicals scavenger, respectively. Therefore, it can be indicated that  $\text{h}^+$  and  $\cdot\text{O}_2^-$  are major active species for the degradation of RhB, and  $\cdot\text{OH}$  plays a secondary role.

Based on the above photocatalytic experiment results and the characterization of  $\text{Bi}_2\text{MoO}_6/\text{MSB}$  composite, the photocatalytic degradation of RhB by  $\text{Bi}_2\text{MoO}_6/\text{MSB}$  composite photocatalyst under visible light irradiation mainly includes the following process:

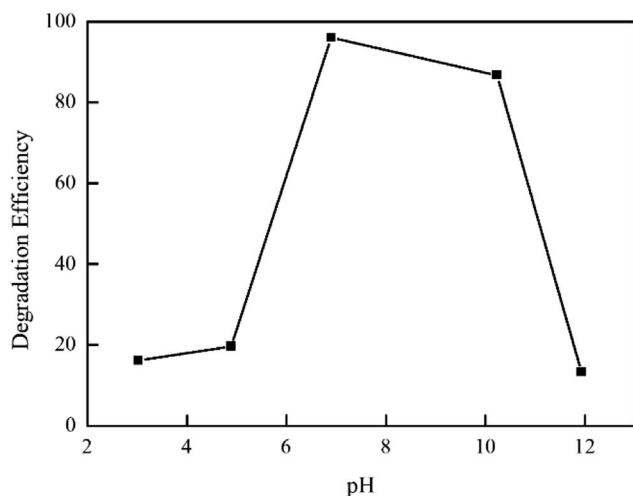
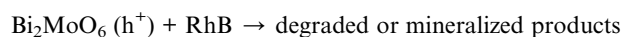
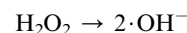
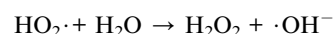
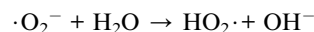
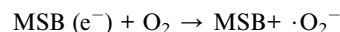
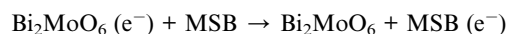
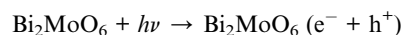


Fig. 9 Effect of pH on Degradation of RhB.



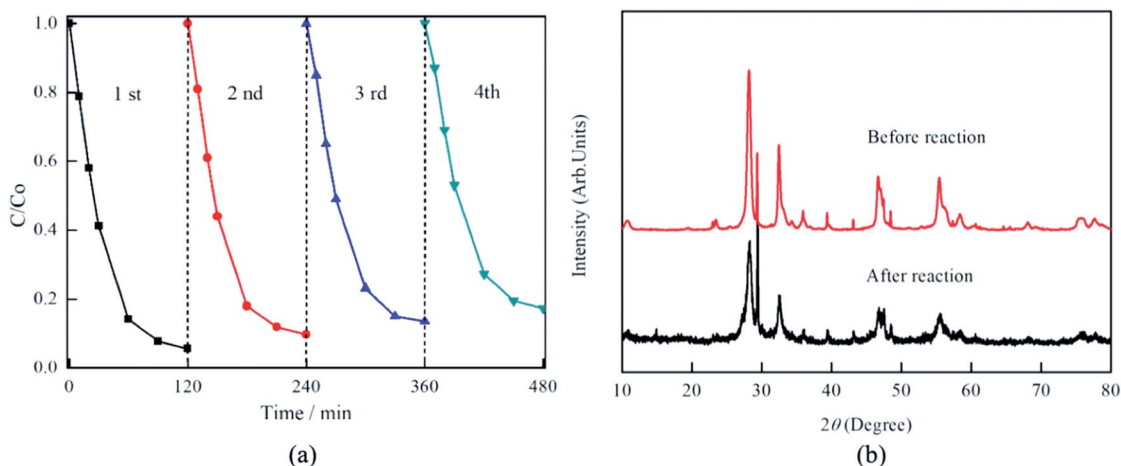


Fig. 10 (a) Photocatalytic degradation of RhB by Bi<sub>2</sub>MoO<sub>6</sub>/MSB composite photocatalysts in different cycling runs, (b) XRD patterns of Bi<sub>2</sub>MoO<sub>6</sub>/MSB before and after cycling photocatalytic test.

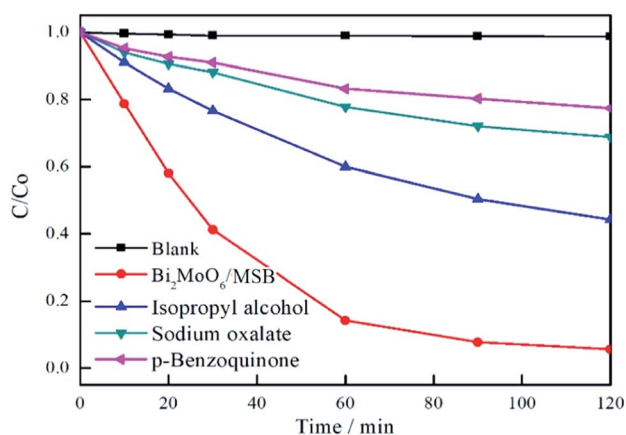


Fig. 11 The effects of photogenerated carriers trapping on photocatalytic degradation activity of Bi<sub>2</sub>MoO<sub>6</sub>/MSB.

The results showed that the introduction of MSB did not widen the optical response range of Bi<sub>2</sub>MoO<sub>6</sub>, and the specific surface area did not increase. Therefore, the improvement of the photocatalytic activity of Bi<sub>2</sub>MoO<sub>6</sub>/MSB can be attributed to the following aspects: (1) MSB has photocatalytic degradation activity on RhB solution. The electrons of Bi<sub>2</sub>MoO<sub>6</sub> are active under visible light irradiation, which makes the electrons jump between valence bands. The generation of the heterojunction structure of MSB and Bi<sub>2</sub>MoO<sub>6</sub> can improve the photo-generated carrier transfer speed and reduce the composite rate of electron-hole pairs, so as to improve the photocatalytic activity of the composite catalyst. (2) Bi<sub>2</sub>MoO<sub>6</sub> nanosheet dispersed on the surface or in the pore of MSB, exposing more photocatalytic active sites, which enhance the photocatalytic activity of composite materials. (3) MSB has special pores and surface structure, which can promote the effective adsorption of RhB by composite photocatalyst and further improve the photocatalytic performance of composite

photocatalyst. (4) MSB has a variety of trace metal elements, which can be used as active sites in photocatalytic reactions to promote the catalytic degradation of Bi<sub>2</sub>MoO<sub>6</sub>/MSB composite photocatalyst.

## 4. Conclusions

In summary, the Bi<sub>2</sub>MoO<sub>6</sub>/MSB composite have been successfully prepared by the hydrothermal synthesis method. The results show that Bi<sub>2</sub>MoO<sub>6</sub>/MSB composite consists of *ortho*-phase Bi<sub>2</sub>MoO<sub>6</sub> and calcite CaCO<sub>3</sub>, and no other phase appears. With the addition of MSB, the space structure of Bi<sub>2</sub>MoO<sub>6</sub> is transformed from a hollow spherical structure into a lamellar structure assembled by nano-particle, and the specific surface area is reduced. The Bi<sub>2</sub>MoO<sub>6</sub>/MSB composite photocatalyst absorb in both ultraviolet and visible light area. The Bi<sub>2</sub>MoO<sub>6</sub>/MSB composite photocatalyst exhibited remarkable photocatalytic activity in degrading RhB than the pure Bi<sub>2</sub>MoO<sub>6</sub>. At 120 min of visible light irradiation, the degradation rate was 94.4%, which was 1.36 times as high as pure Bi<sub>2</sub>MoO<sub>6</sub>. Moreover, the Bi<sub>2</sub>MoO<sub>6</sub>/MSB composite photocatalyst has good stability and reusability. The improvement of photocatalytic performance of Bi<sub>2</sub>MoO<sub>6</sub>/MSB composite photocatalyst is related to the heterojunction generation, MSB structure, and trace metal elements in MSB. The addition of MSB can not only improve the photocatalytic activity of composite photocatalyst but also effectively reduce the cost. Therefore, Bi<sub>2</sub>MoO<sub>6</sub>/MSB composite photocatalyst is expected to be used in many fields.

## Conflicts of interest

There are no conflicts to declare.

## Acknowledgements

This study was supported by the State Scholarship Fund of China, Key Research and Development Projects of Zhejiang





Province of China (No. 2018C02043), Demonstration Project of Marine Economic Innovation and Development of Zhoushan City of China, and Demonstration Project of Marine Economic Innovation and Development of Yantai City of China (No. YHCX-SW-L-201705).

## References

- 1 R. Sandhiya, K. Begum and D. Charumathi, *Int. J. Pharm. Pharm. Sci.*, 2016, **8**, 258–266.
- 2 N. Barka, A. Assabbane, A. Nounah, L. Laanab and Y. A. Ichou, *Desalination*, 2009, **235**, 264–275.
- 3 A. Afkhami and R. Moosavi, *J. Hazard. Mater.*, 2010, **174**, 398–403.
- 4 T. Robinson, G. McMullan, R. Marchant and P. Nigam, *Bioresour. Technol.*, 2001, **77**, 247–255.
- 5 C. Namasivayam and D. Sangeetha, *J. Hazard. Mater.*, 2006, **135**, 449–452.
- 6 N. A. Abdelwahab and M. Emh, *Int. J. Biol. Macromol.*, 2018, **108**, 1035–1044.
- 7 Y. Zhou, H. Zhang, L. Cai, J. Guo, Y. Wang, L. Ji and W. Song, *Materials*, 2018, **11**, 1709.
- 8 K. Dutta, S. Mukhopadhyay, S. Bhattacharjee and B. Chaudhuri, *J. Hazard. Mater.*, 2001, **84**, 57–71.
- 9 V. K. Gupta, D. Pathania, S. Agarwal and P. Singh, *J. Hazard. Mater.*, 2012, **243**, 179–186.
- 10 J. Yu and A. Kudo, *Adv. Funct. Mater.*, 2006, **16**, 2163–2169.
- 11 X. Zhang, Z. Ai, F. Jia and L. Zhang, *J. Phys. Chem. C*, 2008, **112**, 747–753.
- 12 Q. J. Ruan and W. D. Zhang, *J. Phys. Chem. C*, 2009, **113**, 4168–4173.
- 13 Y. Liu, Z. Wang, B. Huang, K. Yang, X. Zhang, X. Qin and Y. Dai, *Appl. Surf. Sci.*, 2010, **257**, 172–175.
- 14 L. Guo, K. L. Zhang, H. Shen, C. Wang, Q. Zhao, D. Wang and Y. Liang, *Chem. Eng. J.*, 2019, **370**, 1522–1533.
- 15 M. Zhang, C. Shao, P. Zhang, C. Su, X. Zhang, P. Liang and Y. Liu, *J. Hazard. Mater.*, 2012, **225**, 155–163.
- 16 Y. Chen, G. Tian, Y. Shi, Y. Xiao and H. Fu, *Appl. Catal., B*, 2015, **164**, 40–47.
- 17 W. Wei, Y. Dai and B. Huang, *J. Phys. Chem. C*, 2009, **113**, 5658–5663.
- 18 G. Tian, Y. Chen, R. Zhai, J. Zhou, W. Zhou, R. Wang and H. Fu, *J. Mater. Chem. A*, 2013, **1**, 6961–6968.
- 19 G. Tian, Y. Chen, W. Zhou, K. Pan, Y. Dong, C. Tian and H. Fu, *J. Mater. Chem.*, 2011, **21**, 887–892.
- 20 C. Kongmark, R. Coulter, S. Cristol, A. Rubbens, C. Pirovano, A. Löfberg and R. N. Vannier, *Cryst. Growth Des.*, 2012, **12**, 5994–6003.
- 21 L. Guo, Q. Zhao, H. Shen, X. Han, K. Zhang, D. Wang and B. Xu, *Catal. Sci. Technol.*, 2019, **9**, 3193–3202.
- 22 Z. Lin, W. Wang and L. Zhang, *J. Mol. Catal. A: Chem.*, 2007, **268**, 195–200.
- 23 M. Cao, P. Wang, Y. Ao, C. Wang and J. Hou, *Chem. Eng. J.*, 2015, **264**, 113–124.
- 24 Y. J. Jang, Y. H. Jang and D. H. Kim, *Sci. Adv. Mater.*, 2015, **7**, 956–963.
- 25 S. Ragupathy, K. Raghu and P. Prabu, *Spectrochim. Acta, Part A*, 2015, **138**, 314–320.
- 26 M. J. Sampaio, C. G. Silva, A. M. Silva, L. M. Pastrana-Martinez, C. Han, S. Morales-Torres and J. L. Faria, *Appl. Catal., B*, 2015, **170**, 74–82.
- 27 A. Y. Shan, T. I. M. Ghazi and S. A. Rashid, *Appl. Catal., A*, 2010, **389**, 1–8.
- 28 V. Vaiano, O. Sacco, D. Sannino and P. Ciambelli, *Appl. Catal., B*, 2015, **170**, 153–161.
- 29 J. J. Wang, Y. H. Jing, T. Ouyang and C. T. Chang, *J. Nanosci. Nanotechnol.*, 2015, **15**, 6141–6149.
- 30 J. R. Kim and E. Kan, *J. Environ. Manage.*, 2016, **180**, 94–101.
- 31 B. Plav, S. Kobe and B. Orel, *Kovine, Zlitine, Tehnol.*, 1999, **33**, 517–521.
- 32 N. Huang and J. Wang, *J. Anal. Appl. Pyrolysis*, 2009, **84**, 124–130.
- 33 I. G. Lodeiro, D. E. Macphee, A. Palomo and A. Fernández-Jiménez, *Cem. Concr. Res.*, 2009, **39**, 147–153.
- 34 A. Phuruangrat, P. Jitrou, P. Dumrongrojthanath, N. Ekthammathat, B. Kuntalue, S. Thongtem and T. Thongtem, *J. Nanomater.*, 2013, 1–8.
- 35 L. Zhang, T. Xu, X. Zhao and Y. Zhu, *Appl. Catal., B*, 2010, **98**, 138–146.
- 36 M. Kruk and M. Jaroniec, *Chem. Mater.*, 2001, **13**, 3169–3183.
- 37 B. J. Becker, F. J. Fodrie, P. A. McMillan and L. A. Levin, *Limnol. Oceanogr.*, 2005, **50**, 48–61.
- 38 A. Martínez-de la Cruz, S. O. Alfaro, E. L. Cuéllar and U. O. Méndez, *Catal. Today*, 2007, **129**, 194–199.
- 39 F. Zhou, R. Shi and Y. Zhu, *J. Mol. Catal. A: Chem.*, 2011, **340**, 77–82.
- 40 D. Ma, J. Wu, M. Gao, Y. Xin and C. Chai, *Chem. Eng. J.*, 2017, **316**, 461–470.
- 41 B. Liu, X. Liu, M. Ni, C. Feng, X. Lei, C. Li and L. Pan, *Appl. Surf. Sci.*, 2018, **453**, 280–287.
- 42 T. Jia, W. Wang, F. Long, Z. Fu, H. Wang and Q. Zhang, *J. Phys. Chem. C*, 2009, **113**, 9071–9077.
- 43 Q. He, Y. Ni and S. Ye, *RSC Adv.*, 2017, **7**, 27089–27099.
- 44 J. Bi, L. Wu, J. Li, Z. Li, X. Wang and X. Fu, *Acta Mater.*, 2007, **55**, 4699–4705.
- 45 W. Zhao, C. Chen, X. Li, J. Zhao, H. Hidaka and N. Serpone, *J. Phys. Chem. B*, 2002, **106**, 5022–5028.
- 46 L. Cai, J. Gong, J. Liu, H. Zhang, W. Song and L. Ji, *Materials*, 2018, **11**, 267.
- 47 Z. He, L. Xie, J. Tu, S. Song, W. Liu, Z. Liu and J. Chen, *J. Phys. Chem. C*, 2009, **114**, 526–532.
- 48 Y. Ou, J. D. Lin, H. M. Zou and D. W. Liao, *J. Mol. Catal. A: Chem.*, 2005, **241**, 59–64.
- 49 M. Ge, Y. Li, L. Liu, Z. Zhou and W. Chen, *J. Phys. Chem. C*, 2011, **115**, 5220–5225.
- 50 F. Fu, H. Shen, X. Sun, W. Xue, A. Shoneye, J. Ma and J. Tang, *Appl. Catal., B*, 2019, **247**, 150–162.

